Atomic-scale evidence for highly selective electrocatalytic N–N coupling on metallic MoS_2

Daoping He[a,b,c], Hideshi Ooka[a], Yujeong Kim[d,e], Yamei Li[b], Fangming Jin[c,1], Sun Hee Kim[d,e,1], and Ryuhei Nakamura[a,b,1]

[a]Biofunctional Catalyst Research Team, RIKEN Center for Sustainable Resource Science, Saitama 351-0198, Japan; [b]Earth-Life Science Institute, Tokyo Institute of Technology, 152-8550 Tokyo, Japan; [c]School of Environmental Science and Engineering, State Key Laboratory of Metal Matrix Composites, Shanghai Jiao Tong University, Shanghai 200240, People's Republic of China; [d]Western Seoul Center, Korea Basic Science Institute, Seoul 03759, Republic of Korea; and [e]Department of Chemistry and Nano Science, Ewha Womans University, Seoul 03760, Republic of Korea

Edited by Catherine J. Murphy, University of Illinois at Urbana–Champaign, Urbana, IL, and approved October 28, 2020 (received for review April 30, 2020)

Molybdenum sulfide (MoS_2) is the most widely studied transition-metal dichalcogenide (TMDs) and phase engineering can markedly improve its electrocatalytic activity. However, the selectivity toward desired products remains poorly explored, limiting its application in complex chemical reactions. Here we report how phase engineering of MoS_2 significantly improves the selectivity for nitrite reduction to nitrous oxide, a critical process in biological denitrification, using continuous-wave and pulsed electron paramagnetic resonance spectroscopy. We reveal that metallic 1T-MoS_2 has a protonation site with a pK_a of ∼5.5, where the proton is located ∼3.26 Å from redox-active Mo site. This protonation site is unique to 1T-MoS_2 and induces sequential proton–electron transfer which inhibits ammonium formation while promoting nitrous oxide production, as confirmed by the pH-dependent selectivity and deuterium kinetic isotope effect. This is atomic-scale evidence of phase-dependent selectivity on MoS_2, expanding the application of TMDs to selective electrocatalysis.

denitrification | ENDOR spectroscopy | molybdenum sulfide | phase transitions | electrochemistry

Transition-metal dichalcogenides (TMDs) have gained considerable attention in recent years due to their variable crystal phases, which allow for precise tuning of their electronic, optical, magnetic, and catalytic properties (1, 2). For example, molybdenum sulfide (MoS_2), which is one of the most extensively studied TMDs, exists as different polymorphs depending on the orientation of sulfur atoms around the molybdenum center. In octahedral coordination (1T phase), MoS_2 exhibits metallic behavior, whereas the material acts as a semiconductor in trigonal prismatic coordination (2H phase) (3–6). In addition to higher conductivity, 1T-MoS_2 has enlarged layer spacing and more electrochemical active sites (7, 8), making it a promising next-generation material for batteries (9, 10), memristors (11, 12), capacitors (13, 14), and numerous other energy-related applications (15–17).

In the field of electrocatalysis, phase engineering has mainly been used to enhance catalytic activity. For instance, exchanging 2H-MoS_2 for 1T-MoS_2 results in a marked increase toward the hydrogen evolution reaction (18, 19). Considering the advantage of TMDs being able to control the atomic-scale structure, phase engineering may also open possibilities to control the selectivity of multielectron/proton reactions with multiple possible products, such as CO_2 reduction (20–23), denitrification (NO_3^-/NO_2^- reduction) (24–26), and the electrosynthesis of functional molecules (27–30). Selectivity is a critical requirement for cascade catalysis, one-pot reaction systems, and multistep catalytic processes, and strategies to guide the complex chemical reaction network toward the desired end product are necessary (31, 32). However, to the best of our knowledge, no studies have attempted to exploit the advantages of phase-engineered materials for selective electrocatalysis.

One effective approach to explore phase-engineered MoS_2 for selectivity control is to utilize the newly proposed concept of sequential proton–electron transfer (SPET) (off-diagonal pathways, Fig. 1*A*) (33, 34). In contrast to the extensively studied concerted proton–electron transfer (CPET) pathway, the energy landscape of sequential (decoupled) proton–electron transfer (SPET) pathways is pH-dependent (Fig. 1*B*). This leads to pH-dependent reaction rates (Fig. 1*C*), where the maximum reaction rate can be obtained at a pH close to the pK_a of the reaction intermediate (33, 34). This was recently observed experimentally for nitrite reduction to dinitrogen – an artificial analog of biological denitrification – on partially oxygenated molybdenum sulfide (oxo-MoS_x), and the record high selectivity toward dinitrogen was achieved by simple pH optimization (35). In contrast, this pH dependence was absent in the case of crystalline 2H-MoS_2, demonstrating that the SPET pathway is a unique property of oxo-MoS_x and is therefore probably phase-dependent. However, the origin of the SPET behavior on this material remains unclear. Therefore, elucidating the mechanism at the atomic level would help rationalize the relationship between selectivity and crystal phases, thus providing significant insight into the newly proposed SPET mechanism (33, 34) to enhance the selectivity of multistep electrochemical processes.

Here, we identified the atomic-scale origin of SPET-driven selectivity on MoS_2 using continuous-wave electron paramagnetic resonance (CW-EPR), Raman, and pulsed $^1H/^2H$ electron–nuclear

Significance

Molybdenum sulfide (MoS_2) is the most studied two-dimensional (2D) material bar graphene. Current research on crystal-phase engineering focuses almost exclusively on the improvement of catalytic activity. However, the potential advantages of phase engineering toward regulation of selectivity control during multistep catalytic processes remain unexplored. Here, we report atomic-scale evidence on how metallic MoS_2 shows significantly higher selectivity compared to the semiconducting phase during multielectron reduction of nitrite to nitrous oxide. Namely, a reaction intermediate specific to metallic MoS_2 increases the selectivity by decoupling the proton and electron transfer steps. This has previously been shown to be a universal mechanism to enhance selectivity, and therefore, our work opens directions of the application of 2D materials toward selective electrocatalysis.

Author contributions: D.H. and R.N. designed research; D.H. and Y.K. performed research; D.H., H.O., Y.K., Y.L., F.J., S.H.K., and R.N. analyzed data; and D.H., H.O., S.H.K., and R.N. wrote the paper.

The authors declare no competing interest.

This article is a PNAS Direct Submission.

[1]To whom correspondence may be addressed. Email: fmjin@sjtu.edu.cn, shkim7@kbsi.re.kr, or ryuhei.nakamura@riken.jp.

This article contains supporting information online at https://www.pnas.org/lookup/suppl/doi:10.1073/pnas.2008429117/-/DCSupplemental.

First published November 30, 2020.

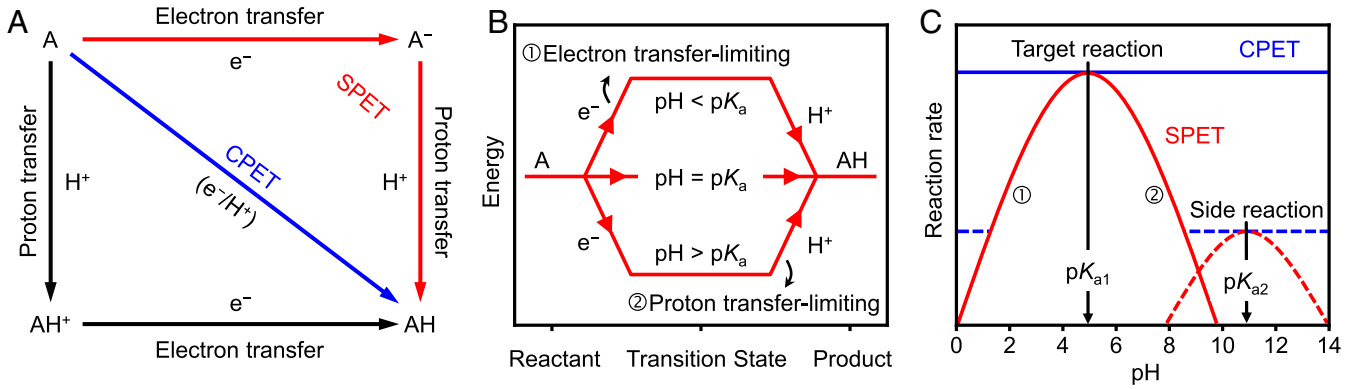

Fig. 1. Selectivity control of MoS_2 based on SPET theory. (*A*) Diagram showing the possible pathways for proton–electron transfer on MoS_2. In the blue pathway (CPET), protons and electrons are transferred in a single elementary step. In contrast, stepwise pathways (SPET) generate an intermediate whose charge depends on whether the electron or proton transfers first (red and black pathways, respectively). (*B*) Diagram showing the energetic landscape of SPET. The landscape depends on the relationship between the pK_a of the reaction intermediate and the solution pH. (*C*) Influence of pH on reaction selectivity. The rates of SPET reactions (red lines) show a pH dependence with a maximum corresponding to the pK_a of the intermediate. Therefore, the relative rate of one reaction over another can be tuned by changing the pH. In contrast, the rate of CPET reactions are pH-independent, and therefore, their relative rates are also constant with respect to pH.

double-resonance (ENDOR) spectroscopy. Specifically, a proton located at the first coordination sphere (~3.26 Å) of a redox-active Mo center was found to have a pK_a value matching that involved in the pH-dependent electrocatalytic selectivity and H/D kinetic isotope effect (KIE). The observed pH-dependent behavior is specific to 1T-MoS_2, as oxo-MoS_x was assigned to the 1T phase using high-resolution transmission electron microscopy (HRTEM), Raman- and X-ray photoelectron spectroscopy (XPS). These results not only provide atomic-scale evidence of SPET in heterogeneous catalysis, but also demonstrate how the phase engineering of TMDs can be used to enhance their electrocatalytic selectivity.

Results and Discussion

Synthesis and Characterization of MoS_2. oxo-MoS_x was synthesized hydrothermally according to a previously reported procedure (35, 36). Briefly, equimolar amounts of molybdate and L-cysteine were mixed and heated inside a Teflon-lined autoclave at 200 °C for 24 h.

An HRTEM image of the as-synthesized material is shown in Fig. 2*A*. Comparison of the obtained HRTEM image with that of commercial 2H-MoS_2 (Fig. 2*D*) revealed differences in the atomic arrangement along the basal plane. This difference was quantified using intensity profiles generated along the colored lines indicated in the HRTEM images (Fig. 2 *A* and *D*). In the case of oxo-MoS_x, only the peaks derived from Mo were observed in the intensity profile (Fig. 2*B*). This finding is consistent with the coordination of S atoms in an octahedron, as found in 1T-MoS_2 (Fig. 2*G*) (37, 38). In contrast, 2H-MoS_2 showed alternating Mo–S peaks (Fig. 2*E*) due to the overlapping of two sulfur atoms along the direction of the electron beam (Fig. 2*G*). To quantify the percentage of the 1T phase in the synthesized oxo-MoS_x, XPS measurements were performed (Fig. 2 *C* and *F* and *SI Appendix*, Fig. S1 and Table S1). The binding energy of the Mo 3*d* peaks in 1T-MoS_x (Fig. 2*C*) was ~1 eV lower than that in 2H-MoS_2 (Fig. 2*F*), which is consistent with the previously reported binding energy of Li-intercalated 1T-MoS_2 (39, 40). The 1T phase percentage was determined to be ~55% from the deconvolution of the Mo *3d* spectra and is close to the phase purity previously achieved using hydrothermal synthesis (37, 41–47). The ratio of Mo:S in oxo-MoS_x was determined to be 1:1.9, which is consistent with the composition of MoS_2, and hence, the as-synthesized oxo-MoS_x is hereafter denoted as 1T-MoS_2. The structures of 1T-MoS_2 and 2H-MoS_2 were also analyzed by Raman (Fig. 2*H*) and ultraviolet-visible (UV-vis) spectroscopy (Fig. 2*I*). The Raman peaks at 150 (J_1), 239 (J_2), and 337 cm^{-1} (J_3) (11, 48–50), and the monotonic change of the UV-vis spectrum (41, 51) are also consistent with the formation of the metallic 1T phase (for more details, see *SI Appendix*, Figs. S2 and S3).

pH-dependent NO_2^- Reduction on MoS_2. The selectivity of 1T-MoS_2 and 2H-MoS_2 toward electrochemical NO_2^- reduction was investigated in a three-electrode H-type cell. The reduction of NO_2^- to N_2O ($2NO_2^- + 4e^- + 6H^+ \rightarrow N_2O + 3H_2O$) is a four-electron, six-proton multistep reaction and the N–N coupling from NO to N_2O (equation 2 in Fig. 3) is a critical step to detoxify NO_2^- to harmless dinitrogen (Fig. 3, bold red lines). The catalysts to convert nitrite to dinitrogen is of considerable practical importance, as nitrate and nitrite are ubiquitous as environmental pollutants (25). However, the N–N coupling in this reaction strongly competes with NH_4^+ production ($NO_2^- + 8H^+ + 6e^- \rightarrow NH_4^+ + 2H_2O$, $NO + 6H^+ + 5e^- \rightarrow NH_4^+ + H_2O$) (Fig. 3, bold blue lines). The selectivity and reaction rate of N_2O production on 1T-MoS_2 and 2H-MoS_2 at 0.1 V versus a reversible hydrogen electrode (RHE) is shown in Fig. 4 *A* and *B* (*SI Appendix*, Fig. S4). For 1T-MoS_2 (red symbols), the Faradaic efficiency (FE) toward N_2O exhibited a clear volcano-type pH dependence with a local maximum at pH 5, providing the maximum FE to date of 42% at near-neutral pH. The formation rate of N_2O also exhibited a maximum at pH 5. Meanwhile, the formation of the NH_4^+ byproduct was effectively suppressed at pH 5 (*SI Appendix*, Fig. S5). The conversion ratio of NO to N_2O reaches 93% based on the reaction rate of N_2O and NH_4^+ (equations 2 and 4 in Fig. 3) at pH 5. In the case of 2H-MoS_2, however, the FE and formation rate of N_2O were pH-independent (Fig. 4 *A* and *B*, blue symbols). The FE of N_2O for 2H-MoS_2 is lower than 5%, and NH_4^+ dominated the products in the entire pH range investigated (Faradaic efficiency > 70%, *SI Appendix*, Fig. S5).

pH-dependent KIE. To evaluate the role of protons in the selectivity of denitrification, the KIE of NO_2^- reduction was evaluated in a deuterated solution by measuring the amount of N_2O generated after 4 h (Fig. 4*C*). In the case of 2H-MoS_2, the KIE is ≥ 1.2 at pH 4.5 and 5, indicating that proton transfer is involved in the rate-limiting step of N_2O formation. In the case of 1T-MoS_2, the KIE was constant at ~1.0 below pH 5.5, but gradually decreased at

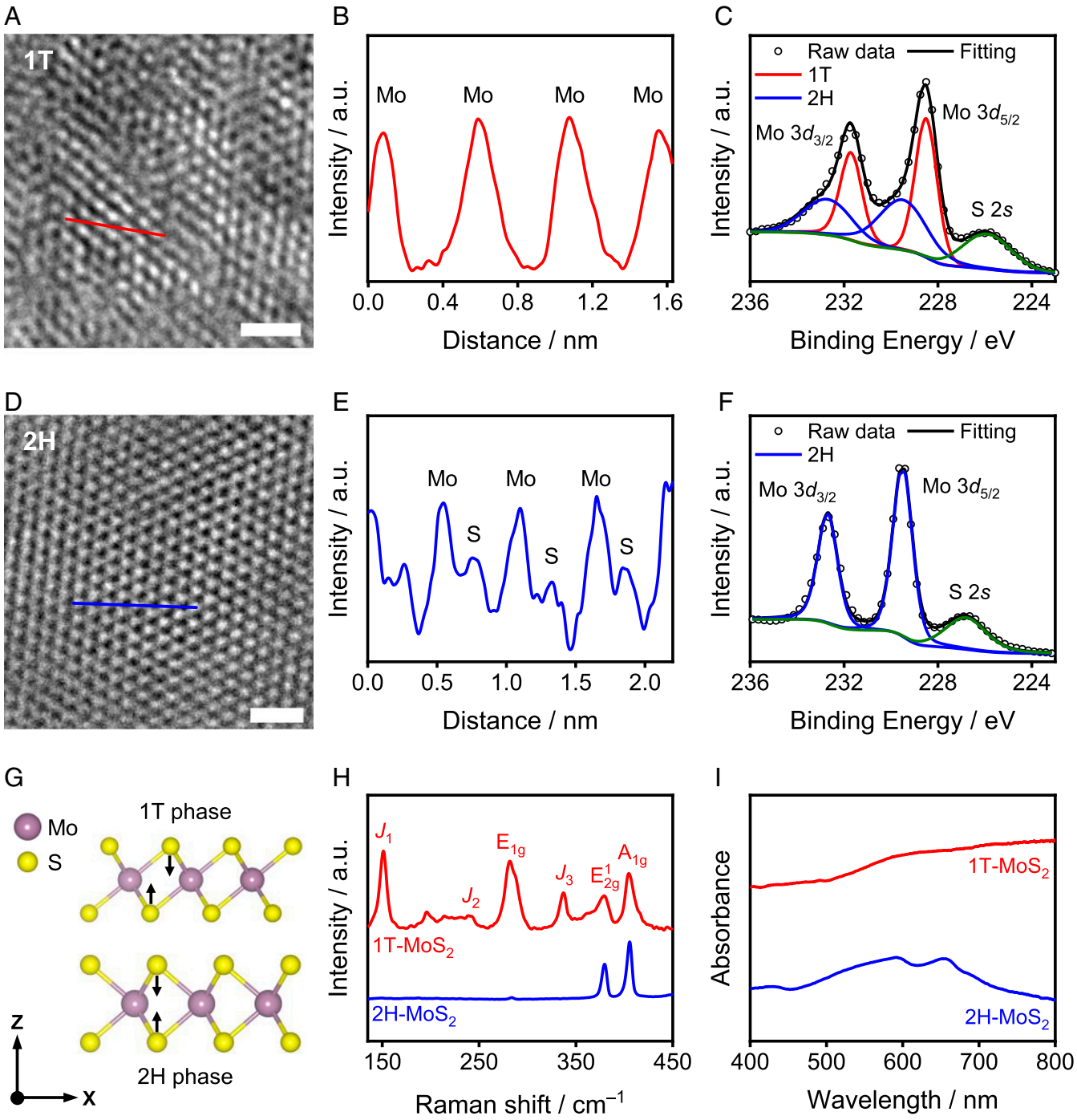

Fig. 2. Structural characterization of 1T-MoS_2 and 2H-MoS_2. (*A* and *D*) HRTEM images of 1T-MoS_2 (*A*) and 2H-MoS_2 (*D*). (Scale bars of *A* and *D*, 1 nm.) (*B* and *E*) The intensity profiles obtained along the red and blue lines in *A* and *D*, respectively. (*C* and *F*) The Mo 3*d* XPS spectra of 1T-MoS_2 (*C*) and 2H-MoS_2 (*F*) along with the spectral deconvolution. (*G*) Schematic representation of 1T and 2H structures. (*H*) Raman spectra, and (*I*) UV-vis spectra of 1T-MoS_2 and 2H-MoS_2.

higher pH, demonstrating the presence of two distinct pH regions. Namely, proton transfer is not involved in the rate-limiting step of N_2O formation below pH 5.5, but is involved at pH ≥ 6. The border between the two pH regions is pH 5.5, a value that coincides with the optimal pH of electrochemical N_2O production (Fig. 4 *A* and *B*).

The observed difference in the pH dependence of selectivity and the KIE can be explained by considering that an electron and a proton are transferred simultaneously (CPET) during the rate-limiting step of 2H-MoS_2, whereas they are decoupled (SPET) in the case of 1T-MoS_2 (Fig. 1*A*). Although SPET has traditionally been considered to be less desirable for electrocatalysis due to the generation of high-energy intermediates (53–55), the theoretical model proposed by Koper suggests that SPET may have unique advantages, such as the pH-dependent suppression of side reactions (33, 34, 56). Fig. 1*B* shows the energy landscape of SPET pathway at equilibrium. When the pH is lower than the pK_a of the reaction intermediate, proton transfer is thermodynamically favored, and the rate-limiting step

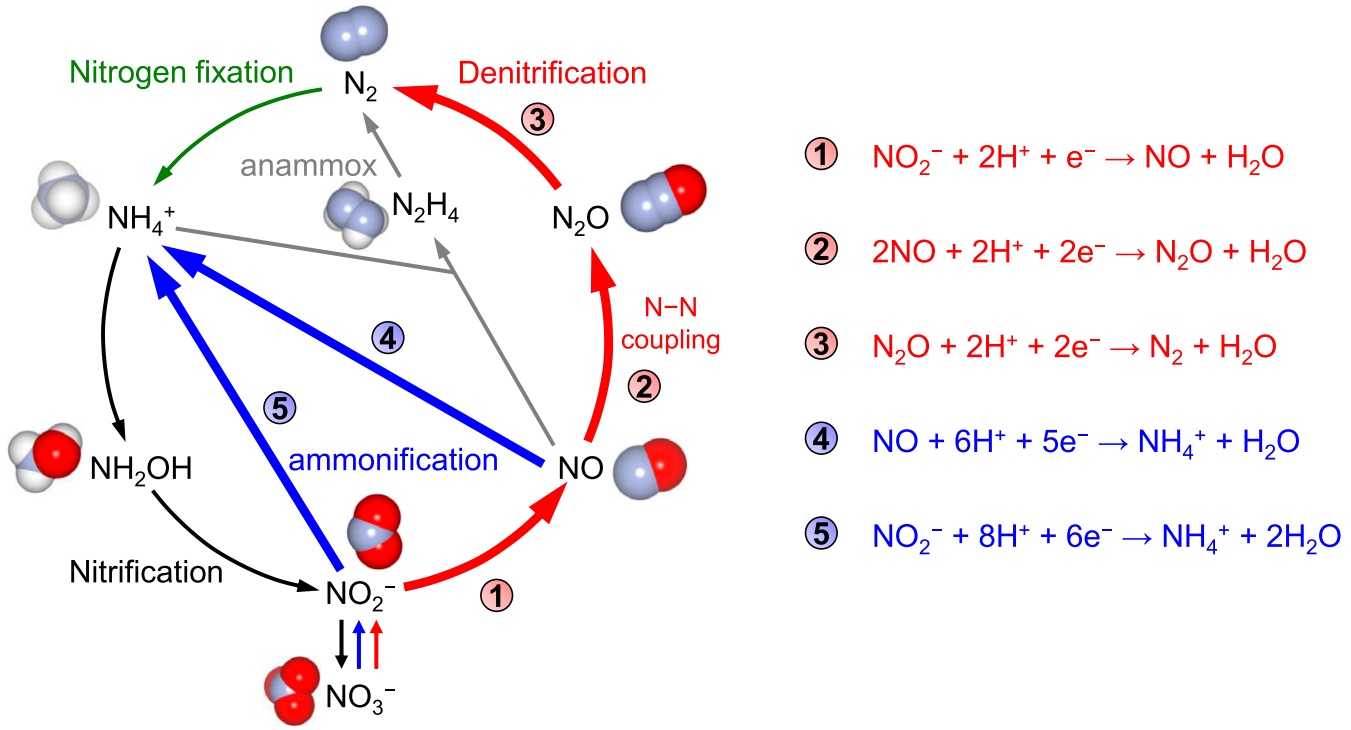

Fig. 3. Major processes of the biological (52) and artificial (24) nitrogen cycle. Denitrification, red arrows; nitrogen fixation, green arrow; nitrification, black arrows; assimilatory ammonification, blue arrows; anaerobic ammonium oxidation (anammox reaction), gray arrows. The redox processes associated with this study are indicated in bold arrows.

is electron transfer. On the other hand, at pH values higher than the pK_a of the intermediate, proton transfer becomes thermodynamically uphill and rate-limiting. Thus, the reaction rates exhibit a pH dependence that reaches a maximum at a pH value close to the pK_a of the reaction intermediate (Fig. 1*C*) (34) and results in a KIE of 1 at pH below the pK_a and a deviation at higher pHs. These predictions are consistent with the results obtained here for 1T-MoS_2 (Fig. 4). In the case of CPET, however, protons and electrons are transferred simultaneously, meaning that only the total driving force (electrode potential vs. RHE) influences the reaction rate. The pH has no effect on the reaction rate if the total driving force is maintained constant as in our experiments (54, 55). The difference in selectivity between the two crystal phases can be explained by hypothesizing that 2H-MoS_2 induces CPET, whereas 1T-MoS_2 induces SPET. Support for this hypothesis can be obtained if a reaction intermediate with a pK_a close to the optimal pH of N_2O production (pH 5) is generated by 1T-MoS_2.

EPR Detection of Active Species in 1T-MoS_2. To directly confirm the existence of an intermediate that satisfies the pK_a requirement, CW-EPR spectroscopy was performed at pH values ranging from 4 ~ 7. At all examined pHs, 20 mM of dithionite was used as a reductant to activate the catalyst, as described previously (35). The electrochemical potential generated upon adding dithionite was +50 mV vs. RHE, which is close to the electrochemical conditions used for evaluating the pH dependence of selectivity (Fig. 4). The CW-EPR experiments were performed at 30 K, where peak splitting was clearly observed (*SI Appendix*, Fig. S6).

The addition of dithionite increased the X-band (9.64 GHz) CW-EPR signals in the range of 350 ~ 370 mT between pH 4 and 7 (Fig. 5, black lines). These signals were assigned to Mo^V species with oxo ligands based on the similarity of the spectral shape and g values with those previously reported for Mo^V oxo species (57–60). As these signals were detected only in the presence of dithionite (*SI Appendix*, Fig. S7), the Mo^V species are predicted to be formed in situ. However, the obtained EPR spectra were clearly influenced by the pH, indicating that the detected Mo^V species are also in a different electronic state. Specifically, the EPR signal with g = [1.966, 1.940, 1.910] at pH ≤ 5.5 is anisotropic, but at pH ≥ 6, the signal becomes isotropic (g = 1.928). This finding further suggests the existence of a protonation site within 1T-MoS_2 with a pK_a of ~5.5. In other words, the detected intermediate has a pK_a value that is consistent with the SPET behavior suggested from the pH dependence of the Faradaic efficiency (Fig. 4*A*), reaction rate (Fig. 4*B*), and KIE (Fig. 4*C*).

Simulations of the CW-EPR spectra (Fig. 5, red lines) for 1T-MoS_2 also show a clear transition from anisotropic to isotropic structures at higher pH values, as the rhombic signal with g = [1.966, 1.940, 1.910] obtained at pH 5.5 shifted to an isotropic one (g = 1.928) at pH 6. The maximum concentration of the Mo^V intermediate at pH 5.5 is estimated to be 0.053 mol % based on the EPR calibration (*SI Appendix*, Fig. S8). Further details on the satellite peaks caused by the hyperfine coupling of ^{95}Mo (I = 5/2), as well as the Q-band pulsed electron spin-echo–EPR spectra measured at 34 GHz are presented in *SI Appendix*, Figs. S9 and S10. In contrast to 1T-MoS_2, no changes in the EPR spectra of 2H-MoS_2 were observed by changing the pH (*SI Appendix*, Fig. S11), indicating that the Mo^V intermediate is specific to 1T-MoS_2.

ENDOR Detection of Protons. To directly confirm the location of the proton with respect to the electrochemically active Mo^V species of 1T-MoS_2, ^1H Davies ENDOR spectroscopy, which is ideal for the detection of strongly coupled nuclei (61–63), was performed. We could examine the presence of the exchangeable proton(s) by subtracting the ^1H ENDOR spectrum obtained in D_2O solution from that obtained in H_2O. In the pH region from 4.0 to 5.5, the subtracted ^1H Davies ENDOR spectra of 1T-MoS_2 contained a signal with a hyperfine coupling value of 3.9 MHz at

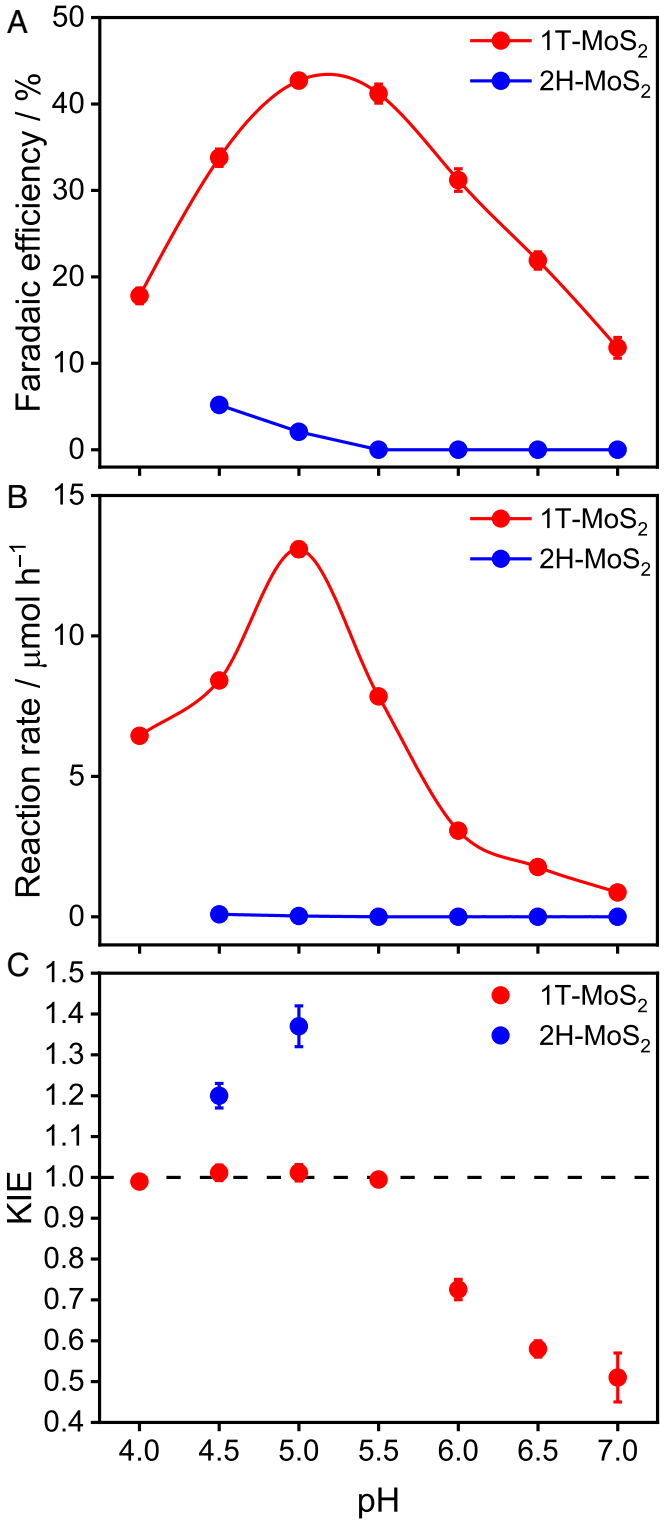

Fig. 4. Electroreduction of NO_2^- to N_2O on MoS_2. (*A*) Faradaic efficiency, (*B*) reaction rate, and (*C*) KIE of N_2O production via NO_2^- reduction (0.1 M) by 1T-MoS_2 and 2H-MoS_2 as a function of pH at 0.1 V vs. RHE for 4 h. Error bars correspond to the average taken over three independent experiments.

g = 1.966 (Fig. 6*A* and *SI Appendix*, Fig. S12), which was assigned to a proton coupled to a Mo center. Field-dependent ENDOR and corresponding simulations revealed ^{1}H ENDOR signals with a hyperfine coupling tensor for the exchangeable proton of A = [–3.4, 4.5, 2.5] MHz, which corresponds to an isotropic hyperfine coupling value (A_{iso}) of 1.2 MHz and anisotropic hyperfine coupling value (A_{dip}) of [–4.6, 3.3, 1.3] MHz. To confirm the ^{1}H ENDOR results, ^{2}H ENDOR measurements were also conducted in D_2O solution. The ^{2}H Mims ENDOR spectra (Fig. 6*B*), which are sensitive for the detection of weakly coupled nuclei, also contain the corresponding signal (hyperfine coupling value of 0.6 MHz at g = 1.966) with a magnetogyric ratio of ^{1}H/^{2}H ~6.5, confirming that the observed proton is labile. From the A_{dip} values obtained from the simulation, the distance of the proton and the Mo^V center and the angle of O–Mo–H was estimated to be ~3.26 Å and ~115°, respectively, which is reasonable considering the bond lengths of Mo–S (~2.41 Å) and

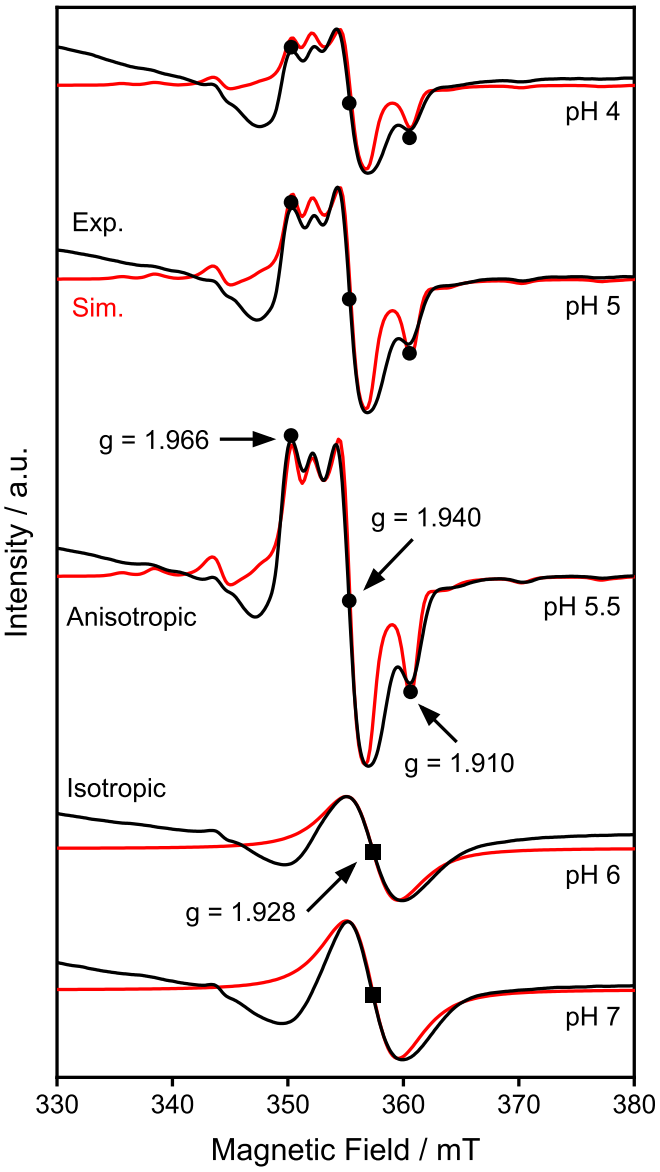

Fig. 5. EPR spectra of 1T-MoS_2. X-band CW-EPR spectra of 1T-MoS_2 generated after reduction by 20 mM dithionite at the indicated pH values (black lines) and the corresponding simulations (red lines). The simulations were performed using the following parameters: g = [1.966, 1.940, 1.910], A = [130, < 50, 175] MHz for pH 4–5.5; g = 1.928 for pH 6–7. Experimental conditions: microwave frequency, 9.64 GHz; microwave power, 1 mW; modulation frequency, 100 kHz; modulation amplitude, 1.0 mT; time constant, 40.96 ms; conversion time, 48.00 ms; sweep time, 96 s; four scans; temperature 30 K.

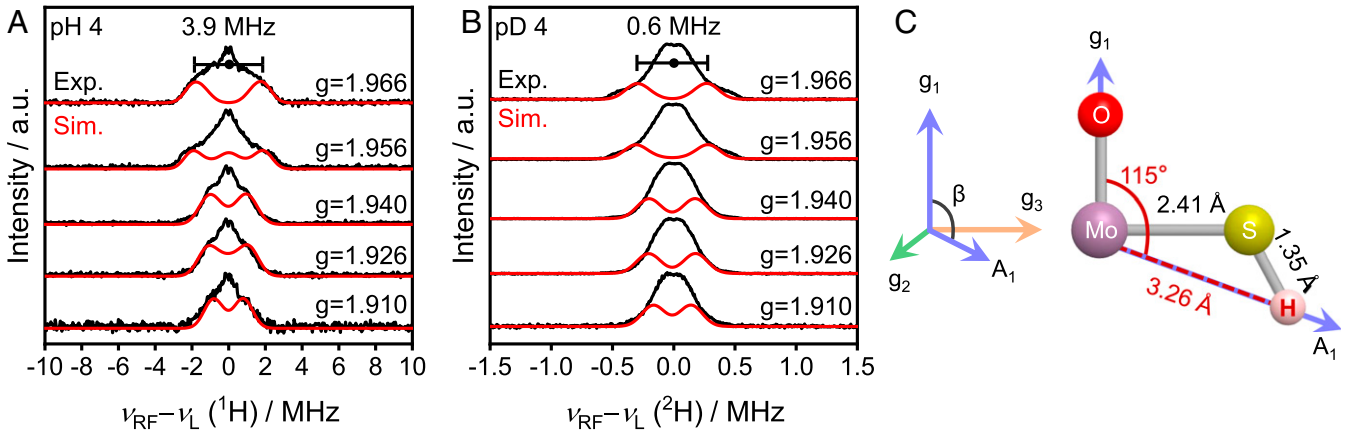

Fig. 6. ENDOR spectra of 1T-MoS_2. (*A*) Two-dimensional field-dependent ^{1}H Davies ENDOR and (*B*) ^{2}H Mims ENDOR spectra of 1T-MoS_2 generated after reduction by 20 mM dithionite at pH 4 (black lines). The simulated spectra are shown in red. The simulation parameters were as follows: *A*: A = [–3.4, 4.5, 2.5] MHz, Euler angle = [α, β, γ] = [90°, 115°, 20°]; *B*: A = [–0.5, 0.7, 0.4] MHz, Euler angle = [α, β, γ] = [90°, 115°, 20°]. (*C*) Schematic of Mo^V site in relation to proton. The distance of the proton to the Mo^V center was estimated to be ~3.26 Å and the angle of O–Mo–H was estimated to be ~115° from the ENDOR simulation. Experimental conditions: microwave frequency, 34 GHz; T = 30 K; Davies ENDOR $\pi/2$ width, 32 ns, τ = 400 ns, radio-frequency pulse width, 20 μs; Mims ENDOR $\pi/2$ width, 32 ns, τ = 200 ns, radio-frequency pulse width, 40 μs.

S–H (~1.35 Å) (48, 64). The location of the labile proton with respect to the Mo^V site, characterized at the atomic scale in this study, is shown schematically in Fig. 6*C*.

Confirmation of the Involvement of 1T Phase. CW-EPR and pulsed ENDOR spectroscopy revealed that SPET is induced by a protonation site with a pK_a of ~5.5, where the proton is located ~3.26 Å from redox-active Mo site. Finally, to ensure that all these spectroscopic observations are indeed specific to metallic 1T phase, we collected Raman spectra under the same conditions used for CW-EPR and ENDOR analysis. Even in the presence of the reductant, the J_1 peak, which is characteristic of the 1T phase, was observed at 155 cm^{-1} in all pH regions examined (Fig. 7*A*, red lines). The J_1 band at 155 cm^{-1} was blueshifted compared to the dried 1T-MoS_2 sample (J_1 at 150 cm^{-1}, Fig. 2*H*), and the peak intensity exhibited the same pH dependence as that observed in the CW-EPR spectra of distorted Mo^V oxo species (Fig. 5). As the blueshift in the J_1 band is consistent with the distortion of the octahedral coordination of the 1T phase (48, 65), the consistency of the pH dependence in the Raman and CW-EPR spectra, as well as the ENDOR detection of protons, corroborate the formation of distorted/anisotropic Mo^V species as a consequence of the SPET reaction. The formation of distorted coordination is also supported by the pH-dependent peak intensity of $E_{2g}{}^1$ (48). The pH dependence of J_1 and $E_{2g}{}^1$ is summarized in Fig. 7*B*. In contrast to 1T-MoS_2, the 2H-MoS_2 showed no clear changes in the Raman spectra ($E_{2g}{}^1$ and A_{1g}), in agreement with the negligible effect of the pH on the selectivity of 2H-MoS_2. In addition, the 1T phase content was determined to be ~57% from the deconvolution of the Mo 3*d* spectra after NO_2^- reduction (*SI Appendix*, Fig. S13), which is close to that before reaction (~55%). Furthermore, we also exclude the possibilities of impurities like MoO_x (66) from XPS data (Fig. 2*C*) and amorphous MoS_x from Raman and electrocatalytic performance (*SI Appendix*, Fig. S14). Thus, we conclude that the SPET behavior, which is the origin for the highly selective N–N coupling, is unique to the atomic arrangement of MoS_2 in the 1T phase.

Conclusions

In summary, we have identified the atomic-scale origin of the phase-dependent selectivity of MoS_2 toward N–N coupling during nitrite reduction, a practically important reaction to restore the balance of the nitrogen cycle. The 1T-MoS_2 can

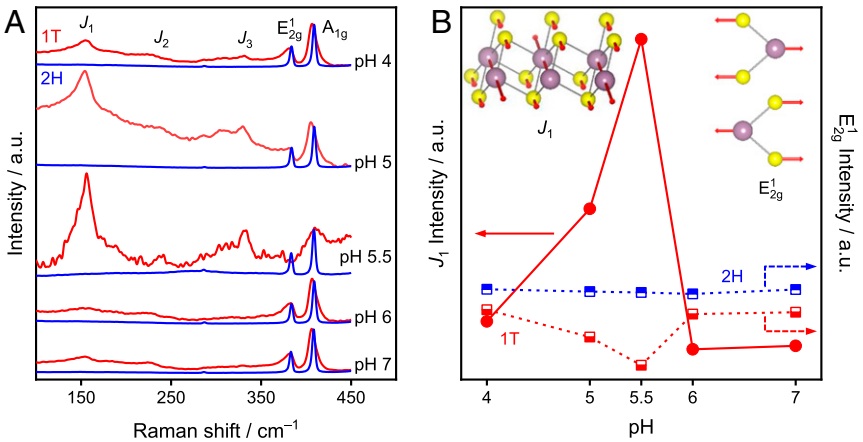

Fig. 7. Raman spectra of MoS_2. (*A*) Raman spectra of 1T-MoS_2 (red lines) and 2H-MoS_2 (blue lines) generated after reduction by 20 mM dithionite at different pH conditions. (*B*) Raman signal intensity of J_1 and $E_{2g}{}^1$ as a function of pH. (*Inset*) The corresponding phonon vibration mode of J_1 and $E_{2g}{}^1$. Experimental conditions: 532-nm laser; coadditions, 20 spectra; integration time, 10 s.

generate N_2O with an FE of up to 42%, which is far superior to 2H-MoS_2 (FE of N_2O < 5%, FE of NH_4^+ > 70%). The pH-dependent CW-EPR and Raman spectra obtained from 1T-MoS_2 provide evidence for a Mo^V intermediate with a pK_a of ~5.5, which is consistent with the SPET behavior suggested from the pH dependence of the FE, reaction rate, and KIE. This intermediate is absent in the case of 2H-MoS_2, which exhibits potential independent selectivity. Taken together, these results unambiguously confirm that a Mo^V intermediate unique to 1T-MoS_2 is responsible for inducing the SPET pathway that promotes N–N coupling in a highly selective manner. Simulations based on the ENDOR spectra indicate that the labile proton is located ~3.26 Å from the redox-active Mo^V center, providing atomic-scale insight into the SPET mechanism to promote the selectivity of complex multistep reactions. This, in turn, demonstrates how the electrocatalytic selectivity of TMDs can be markedly improved by phase engineering, which may further expand their prospects as next-generation materials.

Materials and Methods

Synthesis of 1T-MoS_2. The 1T-MoS_2 was synthesized using the same method as described in our previous report (35). Briefly, 3 mmol of sodium molybdate (Na_2MoO_4, Sigma-Aldrich) and 3 mmol of L-cysteine ($C_3H_7NO_2S$, Wako) were dissolved in 60 mL of ultrapure water (18.2 MΩ, Millipore Ltd.). The solution was stirred for 20 min and subsequently transferred to a Teflon-lined, 100-mL stainless steel autoclave reactor. After hydrothermal treatment at 200 °C for 24 h, the reactor was allowed to cool down naturally to room temperature. The formed black precipitates were collected by filtration and washed with ultrapure water and ethanol alternatively three times. The as-obtained black powder was dried under vacuum (4 Pa) at 60 °C for 12 h.

Crystalline 2H-MoS_2. The 2H-MoS_2 [Molybdenum(IV) Sulfide, Cat. No.: 139–13272] was purchased from Wako Pure Chemical Corporation.

Characterizations. Raman spectra were collected on a Bruker Raman microscopy system (Senterra) using a 532-nm excitation laser. The coadditions of 20 spectra were recorded with an integration time of 10 s. The UV-vis spectra of powder samples were recorded in diffuse transmission mode using a spectrometer (UV-2550, Shimadzu) equipped with a multipurpose large-sample compartment and a built-in integrating sphere (MPC-2200, Shimadzu). X-ray photoelectron spectroscopy (XPS) measurements were performed using a photoelectron spectrometer (AXIS Ultra DLD, Kratos Analytical, Ltd.) with Al Kα radiation. The binding energy was calibrated by setting the C 1*s* peak to 284.6 eV.

Preparation of Working Electrodes. A diluted Nafion solution (0.13 wt %) was prepared by dissolving 50 μL of 10 wt % Nafion solution (Sigma-Aldrich) into a solution containing 3 mL of H_2O and 1 mL of ethanol. The synthesized powder samples (3 mg) were dispersed in 200 μL of the diluted Nafion solution and the mixture was sonicated for about 10 min to generate a homogeneous ink. The ink suspension was transferred onto a carbon paper substrate (EC–TP1–060T, TOYO Corporation) with a geometrical area of 1.5 cm^2 and dried naturally at room temperature before electrolysis experiments.

Electrolysis Experiments and Product Analysis. For electrochemical nitrite reduction under potentiostatic conditions, a two-compartment cell separated by a proton-exchange Nafion perfluorinated membrane (Nafion 117, Sigma-Aldrich) was used. A Ag/AgCl (in a saturated KCl solution) and platinum wire were employed as the reference- and counter electrodes, respectively. The electrolyte consisted of 0.1 M nitrite in either 0.2 M citric acid (at pH 4, 4.5, 5, 5.5) or 0.2 M phosphate buffer (at pH 6, 6.5, 7) solutions. The volume of the electrolyte in the working and counter compartments was 28 and 20 mL, respectively. Prior to electrolysis, the solution in both chambers was bubbled with argon (99.999%) for 30 min to remove dissolved oxygen. All of the potentials were converted to the RHE scale by the equation: $U_{RHE} = U_{Ag/AgCl\ (KCl\ sat.)} + 0.197 + 0.059 \times pH$. During electrolysis, the solution was stirred using a stirring bar at a rate of 500 rpm. After 4 h of electrolysis, the amount of N_2O generated was analyzed by gas chromatography (GC) equipped with a thermal conductivity detector (GC–8APT, Shimadzu). Argon (99.999%) was used as the carrier gas. Ammonium was detected and quantified using commercially available colorimetric titration kits (HACH). The concentration–absorbance calibration curves were obtained using standard ammonia hydrocarbonate solutions, which contained the same concentrations of the buffer used in the electrolysis experiments.

The Faraday efficiency is calculated as follows: Faraday efficiency = $znl/(Q/F)$, where z is the stoichiometric number of electrons consumed for generating 1 mole of product. For nitrite reduction to N_2O and NH_4^+,

$$2NO_2^- + 6H^+ + 4e^- \rightarrow N_2O_{(g)} + 3H_2O (z = 4)$$

$$NO_2^- + 8H^+ + 6e^- \rightarrow NH_4^+ + 2H_2O (z = 6)$$

n is the molar amount of the products determined by gas chromatography, Q is the total charge that passed through the electrochemical cell, and F is the Faraday constant (96,485 C mol^{-1}).

CW-EPR Spectroscopy. X-band (9.64 GHz) CW-EPR spectra were acquired on a Bruker EMX/Plus 6/1 spectrometer equipped with a liquid helium quartz cryostat (Oxford Instruments ESR900) using a temperature and gas flow controller (Oxford Instruments ITC503). The preparation procedures of CW-EPR samples are as follows: 3 mg of catalyst powder was added into 200 μL of a buffer solution (Buffer solution was prepared using either 0.2 M citric acid (Wako, Japan) for pH 4, 5, and 5.5, or 0.2 M phosphate [Wako] for pH 6 and 7, respectively) and the mixture was sonicated for 5 min to generate a homogeneous suspension. After purging the suspension with N_2 to remove the dissolved oxygen, 8.3 μL of a 0.5 M dithionite (Sigma-Aldrich) solution was added under N_2 bubbling to reduce the catalyst. After 5 min, 20 μL of glycerol (Sigma-Aldrich) was added and 200 μL of the suspension was transferred to a CW-EPR tube and frozen in liquid nitrogen immediately. The CW-EPR spectra were collected under the following experimental conditions: microwave frequency, 9.64 GHz; microwave power, 1 mW; modulation frequency, 100 kHz; modulation amplitude, 1.0 mT; time constant, 40.96 ms; conversion time, 48.00 ms; sweep time, 96 s; four scans; temperature 30 K.

ENDOR Spectroscopy. Q-band (34 GHz) ENDOR measurement was performed on a Bruker Elexsys E580 spectrometer with a cryostat (Oxford CF-935) and an Oxford ITC temperature controller. The data were obtained by an EN5107D2 resonator at 30 K. The ^1H Davies ENDOR spectra were obtained using $\pi–T–\pi/2–\tau–\pi–$echo, with microwave pulse lengths of $t_{\pi/2}$ = 32 ns and an interpulse time of τ = 400 ns. The radio-frequency pulse length (T) was 20 μs. The ^2H Mims ENDOR spectroscopy was carried out by a sequence of $\pi/2–\tau–\pi/2–T–\pi/2–$echo ($t_{\pi/2}$ = 32 ns, τ = 200 ns, and T = 20 μs). All ENDOR spectra were collected by stochastic sampling for a better baseline of the spectra. All of the simulations (CW-EPR, ENDOR) were performed using EasySpin (67).

In Situ Raman Spectroscopy. Raman spectra of MoS_2 were collected on a Bruker Raman microscopy system (Senterra) using a 532-nm excitation laser. For in situ measurements, the surface of a MoS_2 electrode was immersed in a degassed buffer solution with 20 mM dithionite under N_2 atmosphere. The coadditions of 20 spectra were recorded with an integration time of 10 s.

Data Availability. All study data are included in the article and *SI Appendix*.

ACKNOWLEDGMENTS. This work was supported by a Japan Society for the Promotion of Science (JSPS) Grant-in-Aid for Scientific Research (26288092) to R.N. and National Research Foundation of Korea (Grant NRF-2017M3D1A1039380) to S.H.K.

1. M. Chhowalla *et al*., The chemistry of two-dimensional layered transition metal dichalcogenide nanosheets. *Nat. Chem.* **5**, 263–275 (2013).
2. Q. H. Wang, K. Kalantar-Zadeh, A. Kis, J. N. Coleman, M. S. Strano, Electronics and optoelectronics of two-dimensional transition metal dichalcogenides. *Nat. Nanotechnol.* **7**, 699–712 (2012).
3. D. Voiry, A. Mohite, M. Chhowalla, Phase engineering of transition metal dichalcogenides. *Chem. Soc. Rev.* **44**, 2702–2712 (2015).
4. R. Kappera *et al*., Phase-engineered low-resistance contacts for ultrathin MoS_2 transistors. *Nat. Mater.* **13**, 1128–1134 (2014).
5. L. Liu *et al*., Phase-selective synthesis of 1T′ MoS_2 monolayers and heterophase bilayers. *Nat. Mater.* **17**, 1108–1114 (2018).
6. Y. C. Lin, D. O. Dumcenco, Y. S. Huang, K. Suenaga, Atomic mechanism of the semiconducting-to-metallic phase transition in single-layered MoS_2. *Nat. Nanotechnol.* **9**, 391–396 (2014).

7. S. L. Shi, Z. X. Sun, Y. H. Hu, Synthesis, stabilization and applications of 2-dimensional 1T metallic MoS_2. *J. Mater. Chem. A Mater.* **6**, 23932–23977 (2018).
8. C. R. Zhu, D. Gao, J. Ding, D. Chao, J. Wang, TMD-based highly efficient electrocatalysts developed by combined computational and experimental approaches. *Chem. Soc. Rev.* **47**, 4332–4356 (2018).
9. Y. C. Jiao *et al*., Ion transport nanotube assembled with vertically aligned metallic MoS_2 for high rate lithium-ion batteries. *Adv. Energy Mater.* **8**, 1702779 (2018).
10. Y. C. Jeong *et al*., Rational design of exfoliated 1T MoS_2@CNT-based bifunctional separators for lithium sulfur batteries. *J. Mater. Chem. A* **5**, 23909–23918 (2017).
11. P. Cheng, K. Sun, Y. H. Hu, Memristive behavior and ideal memristor of 1T phase MoS_2 nanosheets. *Nano Lett.* **16**, 572–576 (2016).
12. X. Zhu, D. Li, X. Liang, W. D. Lu, Ionic modulation and ionic coupling effects in MoS_2 devices for neuromorphic computing. *Nat. Mater.* **18**, 141–148 (2019).
13. M. Acerce, D. Voiry, M. Chhowalla, Metallic 1T phase MoS_2 nanosheets as supercapacitor electrode materials. *Nat. Nanotechnol.* **10**, 313–318 (2015).
14. X. Geng *et al*., Two-dimensional water-coupled metallic MoS_2 with nanochannels for ultrafast supercapacitors. *Nano Lett.* **17**, 1825–1832 (2017).
15. Z. D. Lei, J. Zhan, L. Tang, Y. Zhang, Y. Wang, Recent development of metallic (1T) phase of molybdenum disulfide for energy conversion and storage. *Adv. Energy Mater.* **8**, 1703482 (2018).
16. H. Y. Li, X. F. Jia, Q. Zhang, X. Wang, Metallic transition-metal dichalcogenide nanocatalysts for energy conversion. *Chem* **4**, 1510–1537 (2018).
17. M. Samadi *et al*., Group 6 transition metal dichalcogenide nanomaterials: Synthesis, applications and future perspectives. *Nanoscale Horiz.* **3**, 90–204 (2018).
18. Y. Huang *et al*., Atomically engineering activation sites onto metallic 1T-MoS_2 catalysts for enhanced electrochemical hydrogen evolution. *Nat. Commun.* **10**, 982 (2019).
19. M. A. Lukowski *et al*., Enhanced hydrogen evolution catalysis from chemically exfoliated metallic MoS_2 nanosheets. *J. Am. Chem. Soc.* **135**, 10274–10277 (2013).
20. R. Kortlever, J. Shen, K. J. Schouten, F. Calle-Vallejo, M. T. Koper, Catalysts and reaction pathways for the electrochemical reduction of carbon dioxide. *J. Phys. Chem. Lett.* **6**, 4073–4082 (2015).
21. M. B. Ross *et al*., Designing materials for electrochemical carbon dioxide recycling. *Nat. Catal.* **2**, 648–658 (2019).
22. Y. Lum, J. W. Ager, Sequential catalysis controls selectivity in electrochemical CO_2 reduction on Cu. *Energy Environ. Sci.* **11**, 2935–2944 (2018).
23. K. D. Yang *et al*., Morphology-directed selective production of ethylene or ethane from CO_2 on a Cu mesopore electrode. *Angew. Chem. Int. Ed.* **56**, 796–800 (2017).
24. V. Rosca, M. Duca, M. T. de Groot, M. T. Koper, Nitrogen cycle electrocatalysis. *Chem. Rev.* **109**, 2209–2244 (2009).
25. M. Duca, M. T. M. Koper, Powering denitrification: The perspectives of electrocatalytic nitrate reduction. *Energy Environ. Sci.* **5**, 9726–9742 (2012).
26. K. Kamiya *et al*., Selective reduction of nitrate by a local cell catalyst composed of metal-doped covalent triazine frameworks. *ACS Catal.* **8**, 2693–2698 (2018).
27. M. D. Kärkäs, Electrochemical strategies for C-H functionalization and C-N bond formation. *Chem. Soc. Rev.* **47**, 5786–5865 (2018).
28. M. Jouny *et al*., Formation of carbon-nitrogen bonds in carbon monoxide electrolysis. *Nat. Chem.* **11**, 846–851 (2019).
29. V. R. Pattabiraman, J. W. Bode, Rethinking amide bond synthesis. *Nature* **480**, 471–479 (2011).
30. T. Wang *et al*., Rational design of selective metal catalysts for alcohol amination with ammonia. *Nat. Catal.* **2**, 773–779 (2019).
31. A. M. Appel *et al*., Frontiers, opportunities, and challenges in biochemical and chemical catalysis of CO_2 fixation. *Chem. Rev.* **113**, 6621–6658 (2013).
32. K. D. Yang, C. W. Lee, K. Jin, S. W. Im, K. T. Nam, Current status and bioinspired perspective of electrochemical conversion of CO_2 to a long-chain hydrocarbon. *J. Phys. Chem. Lett.* **8**, 538–545 (2017).
33. M. T. M. Koper, Theory of multiple proton–electron transfer reactions and its implications for electrocatalysis. *Chem. Sci.* **4**, 2710–2723 (2013).
34. M. T. M. Koper, Volcano activity relationships for proton-coupled electron transfer reactions in electrocatalysis. *Top. Catal.* **58**, 1153–1158 (2015).
35. D. He *et al*., Selective electrocatalytic reduction of nitrite to dinitrogen based on decoupled proton-electron transfer. *J. Am. Chem. Soc.* **140**, 2012–2015 (2018).
36. Y. Li *et al*., Enzyme mimetic active intermediates for nitrate reduction in neutral aqueous media. *Angew. Chem. Int. Ed.* **59**, 9744–9750 (2020).
37. W. Ding *et al*., Highly ambient-stable 1T-MoS_2 and 1T-WS_2 by hydrothermal synthesis under high magnetic fields. *ACS Nano* **13**, 1694–1702 (2019).
38. G. Eda *et al*., Coherent atomic and electronic heterostructures of single-layer MoS_2. *ACS Nano* **6**, 7311–7317 (2012).
39. G. Eda *et al*., Photoluminescence from chemically exfoliated MoS_2. *Nano Lett.* **11**, 5111–5116 (2011).
40. Y. Yin *et al*., Contributions of phase, sulfur vacancies, and edges to the hydrogen evolution reaction catalytic activity of porous molybdenum disulfide nanosheets. *J. Am. Chem. Soc.* **138**, 7965–7972 (2016).
41. Q. Liu *et al*., Gram-scale Aqueous synthesis of stable few-layered 1T-MoS_2: Applications for visible-light-driven photocatalytic hydrogen evolution. *Small* **11**, 5556–5564 (2015).
42. J. Ekspong *et al*., Stable sulfur-intercalated 1T′ MoS_2 on graphitic nanoribbons as hydrogen evolution electrocatalyst. *Adv. Funct. Mater.* **28**, 1802744 (2018).
43. M. A. R. Anjum, H. Y. Jeong, M. H. Lee, H. S. Shin, J. S. Lee, Efficient hydrogen evolution reaction catalysis in alkaline media by all-in-one MoS_2 with multifunctional active sites. *Adv. Mater.* **30**, e1707105 (2018).
44. Z. Sun, M. Yang, Y. Wang, Y. H. Hu, Novel binder-free three-dimensional MoS_2-based electrode for efficient and stable electrocatalytic hydrogen evolution. *ACS Appl. Energy Mater.* **2**, 1102–1110 (2019).
45. F. Z. Wang *et al*., Ammonia intercalated flower-like MoS_2 nanosheet film as electrocatalyst for high efficient and stable hydrogen evolution. *Sci. Rep.* **6**, 31092 (2016).
46. L. Cai *et al*., High-content metallic 1T phase in MoS_2-based electrocatalyst for efficient hydrogen evolution. *J. Phys. Chem. C* **121**, 15071–15077 (2017).
47. D. Z. Wang *et al*., Phase engineering of a multiphasic 1T/2H MoS_2 catalyst for highly efficient hydrogen evolution. *J. Mater. Chem. A* **5**, 2681–2688 (2017).
48. S. Jiménez Sandoval, D. Yang, R. F. Frindt, J. C. Irwin, Raman study and lattice dynamics of single molecular layers of MoS_2. *Phys. Rev. B* **44**, 3955–3962 (1991).
49. Y. Yu *et al*., High phase-purity 1T′-MoS_2- and 1T′-$MoSe_2$-layered crystals. *Nat. Chem.* **10**, 638–643 (2018).
50. Y. Liu *et al*., Chemical activation of hollow carbon nanospheres induced self-assembly of metallic 1T phase MoS_2 ultrathin nanosheets for electrochemical lithium storage. *Electrochim. Acta* **353**, 136545 (2020).
51. X. Geng *et al*., Pure and stable metallic phase molybdenum disulfide nanosheets for hydrogen evolution reaction. *Nat. Commun.* **7**, 10672 (2016).
52. L. B. Maia, J. J. Moura, How biology handles nitrite. *Chem. Rev.* **114**, 5273–5357 (2014).
53. T. Liu *et al*., Accelerating proton-coupled electron transfer of metal hydrides in catalyst model reactions. *Nat. Chem.* **10**, 881–887 (2018).
54. J. J. Warren, T. A. Tronic, J. M. Mayer, Thermochemistry of proton-coupled electron transfer reagents and its implications. *Chem. Rev.* **110**, 6961–7001 (2010).
55. D. R. Weinberg *et al*., Proton-coupled electron transfer. *Chem. Rev.* **112**, 4016–4093 (2012).
56. A. J. Göttle, M. T. M. Koper, Proton-coupled electron transfer in the electrocatalysis of CO_2 reduction: Prediction of sequential *vs.* concerted pathways using DFT. *Chem. Sci.* **8**, 458–465 (2017).
57. P. D. Tran *et al*., Coordination polymer structure and revisited hydrogen evolution catalytic mechanism for amorphous molybdenum sulfide. *Nat. Mater.* **15**, 640–646 (2016).
58. A. J. A. Konings *et al*., ESR studies on hydrodesulfurization catalysts: Supported and unsupported sulfided molybdenum and tungsten catalysts. *J. Catal.* **54**, 1–12 (1978).
59. L. Busetto, A. Vaccari, G. Martini, Electron-spin resonance of paramagnetic species as a tool for studying the thermal-decomposition of molybdenum trisulfide. *J. Phys. Chem.* **85**, 1927–1930 (1981).
60. N. R. Glasser, P. H. Oyala, T. H. Osborne, J. M. Santini, D. K. Newman, Structural and mechanistic analysis of the arsenate respiratory reductase provides insight into environmental arsenic transformations. *Proc. Natl. Acad. Sci. U.S.A.* **115**, E8614–E8623 (2018).
61. D. Kim, N. H. Kim, S. H. Kim, 34 GHz pulsed ENDOR characterization of the copper coordination of an amyloid β peptide relevant to Alzheimer's disease. *Angew. Chem. Int. Ed.* **52**, 1139–1142 (2013).
62. B. M. Hoffman, ENDOR of metalloenzymes. *Acc. Chem. Res.* **36**, 522–529 (2003).
63. J. Yano, K. Sauer, J. J. Girerd, V. K. Yachandra, Single crystal X- and Q-band EPR spectroscopy of a binuclear Mn_2(III,IV) complex relevant to the oxygen-evolving complex of photosystem II. *J. Am. Chem. Soc.* **126**, 7486–7495 (2004).
64. A. Singh, A. K. Singh, Origin of *n*-type conductivity of monolayer MoS_2. *Phys. Rev. B* **99**, 121201 (2019).
65. A. P. Nayak *et al*., Pressure-dependent optical and vibrational properties of monolayer molybdenum disulfide. *Nano Lett.* **15**, 346–353 (2015).
66. S. Hong, C. K. Rhee, Y. Sohn, Photoelectrochemical hydrogen evolution and CO_2 reduction over MoS_2/Si and $MoSe_2$/Si nanostructures by combined photoelectrochemical deposition and rapid-thermal annealing process. *Catalysts* **9**, 494 (2019).
67. S. Stoll, A. Schweiger, EasySpin, a comprehensive software package for spectral simulation and analysis in EPR. *J. Magn. Reson.* **178**, 42–55 (2006).